FAMPO
FEDERATION OF AFRICAN MEDICAL PHYSICS ORGANIZATIONS

African Journal of Medical Physics
2022; 4(1): 96-112. doi: 10

Research Paper

Pressure Dependence of Water 1H Spin Relaxation Rates in Model Hydrogel and Intervertebral Spinal Discs

Wilson M. Egadwa [1, ✉], Mark Pearcy [2] and Konstantin Momot [3]

1. Garissa County Referral Hospital, Garissa, Kenya.
2. School of Mech. Medical & Process Engineering, Queensland University of Technology, Brisbane, Australia
3. Queensland University of Technology, Brisbane, Australia.

✉ Corresponding author: Wilson M. Egadwa, Garissa County Referral Hospital, Garissa, Kenya; Email: wmisigo@gmail.com

ISSN 2643-5977

Received: 2022.10.15; Accepted: 2023.03.21; Published: 2023.07.30

Abstract

Back pain is a major cause of disability. It is estimated that around 540 million people worldwide are currently suffering from back pains. This numbers are likely to increase especially in the low- and middle-income countries which are experiencing an increase in life expectancy. It is projected that 70–90% of people will have to experience some form of back pain in their lifetime with 10% experiencing disability as a result. Spine stiffness, neck and low back ache are the most common forms of back pain. Most cases of lower back pain have been shown to be associated with inter-vertebral disc (IVD) degeneration. MRI is a tool used to qualitatively detect structural deformities to the IVD resulting from degeneration. However, these deformities manifest in the terminal stages of degeneration. A method is needed to improve the sensitivity of MRI to quantitatively measure progression of degeneration from the onset of the disease which can vastly improve treatment outcomes. It has been observed that a reduction in Nucleus Pulpous (NP) hydrostatic pressure is one indicator of disc degeneration and that there is a direct correlation between fluid pressure inside the Nucleus Pulposus and the axial load on the disc. The NP hydrostatic pressure is currently measured using discography; an invasive procedure with the potential to further damage the IVD. Previous studies have also shown that MR spin relaxations rates of water protons are sensitive to mechanical stress on the Nucleus Pulposus. However, it is still not clear whether this is due to changes in the chemical composition due to water efflux or if it is due to hydrostatic pressure per se. In this study, the dependence of spin relaxation times in model connective tissue on the hydrostatic pressure is presented. Samples of Gelatine Hydrogen 90% w/w and 10% w/w and oxtail Nucleus Pulpous were separately subjected to confined axial compressive stresses and analysis of their relaxation rates made. Measurement was done using NMR relaxation imaging and validated using NMR spectroscopy R_1 measurements. R_2 measurements were conducted using Spin Echo technique and FOV of 128 pixel x 128 pixels. From Sync 3 pulse, a series of Free Induction decays were acquired and then Fourier transformed. The area in each spectrum indicated the level of magnetization left after polarization pulse. The integration was implemented by use of Bruker Topspin 1.5 software. Plotting areas as a function of time and fitting was done using custom made Mathematica 4.1 (Wolfram research, Inc.) program to the equations. The measurement outcome was inconclusive, with most parts of the experimental results showing that within physiological pressure alone, in the absence of compositional chemical changes, it is not capable of inducing significant changes in relaxation rates. Further studies are proposed to confirm the results.

Keywords: MRI, Nucleus Pulposus, Hydrostatic pressure, Spin Relaxation.

Introduction

Theoretical Background of Intervetebral Spinal Disc Biology and Mechanics

The IVD is a porro-elastic cylindrical tissue situated in between two adjacent vertebral bodies as shown in Figure 1. It accounts for about 25% of the entire length of vertebral column. Its basic function is to distribute the load on the trunk as well as prevent vertebrae bodies from grinding against each other during normal physiologic functions. As such the integrity of the IVD is critical to the wellbeing of the vertebral column.

The IVD consists of a central Nucleus Pulpous (NP) inside concentric lamellas of Annulus Fibrosus (AF). In the interface between the disc and the vertebral body is the cartilage endplate. Collagen, proteoglycans matrix and water form approximately 90% of the disc volume [1, 2].

Proteoglycans constitute approximately 65% and 20 % of the NP and AF dry weight respectively. The tissue can therefore be considered charged because linked to the PGs are the glycosaminoglycan (GAG) which are negatively charged (SO_3^- and COO^-). The PG and GAG form aggregates which gets enmeshed in collagen network to form a poro-elastic extracellular matrix. The charged matrix creates an electrostatic force which help maintain matrix turgidity.

Nucleus Pulposus (NP)

The Nucleus Pulposus is a gel like material comprising of almost half of the non-degenerate disc. It is primarily 90% water in infants and decrease with advancing age to 70% [3]. The Nucleus Pulposus main function is to redistribute stress concentration during physiologic functions such as trunk flexion and extension.

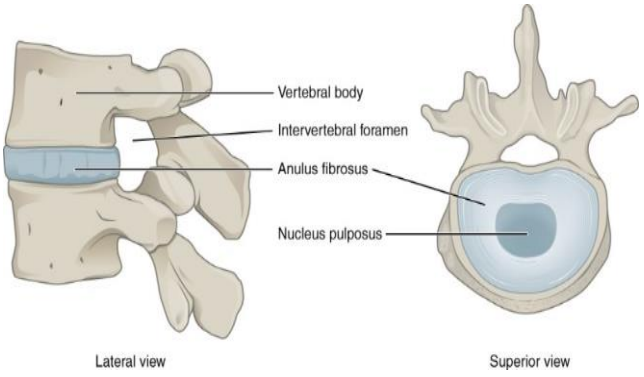

Figure 1. Structure of Intervertebral Disc [Reproduced from: http://en.wikipedia.org/wiki/Intervertebral_disc].

Proteoglycans (PG) constitute about 65 % of the dry weight of the NP [3]. Only about 25% of the proteoglycans are aggregate bound to hyaluronic acid in a sparsely distributed collagen matrix holding the aggrecans. The rest of the PG are freely distributed with no attachment to any site. The glycosaminoglycan's carboxyl and sulphate ions in the PG gives it its hydrophilic attribute explaining the high-water content and the consequent turgidity of the NP [4]. The type 2 Collagen found in the NP consists of elastic fibres and constitutes about 30% of the NP dry matter and they provide the elasticity needed to moderate lateral stretch during compression. There are also traces of matrix synthesising cells located near the nutrient rich cartilage end plate.

Annulus Fibrosus (AF)

Annulus Fibrosus is about 60% water [5]. The AF has 60% collagen fibres in dry weight with 20 % PG dry weight. AF is mainly made up of concentric collagen sheets of bound together by PG gel. The collagen fibres contain chondrocytes and fibroblasts which provide proteoglycan and collagens matrix synthesis. Type 1 collagen is tensile in nature suitable for tension and compressive forces. The AF lamellae are parallel to each other with the fibre's orientation alternating with each subsequent lamellae sheet.

Vertebral Endplate

The vertebral endplate is hyaline cartilage of about 1mm thick that separates the NP and AF from the vertebral body. It is made up of proteoglycans and collagen fibres. The endplate is not homogenous; it has a central part which covers the NP having a high water and PG content while the part overlaying the AF has high collagen and less water content. This regional homogeneity with the NP and AF facilitates easier diffusion of nutrients from the vertebral body.

Metabolism of the IVD

The IVD is metabolically active with enzymes that synthesise and break down its matrix. A balance between the synthesis and breakdown is controlled by other enzymes known as proteinase inhibitors. This shows that any imbalance between synthesis and breakdown of matrix will initiate disc degeneration.

Functions of the Disc

The Nucleus Pulpous hydration is important in the mechanical action of an IVD. Under compression, the NP expands laterally stretching the AF. A higher compressive stress will cause fluids to be expressed from the NP through the AF. This action continues until the compression load is in equilibrium with AF swelling pressure. Reduction of compressive load causes water to be reabsorbed into NP due to its relatively high osmotic potential. With this action it is possible to measure either

mechanically or osmotically the swelling pressure at any compressive load [6].

A disc under sustained compression and without the NP will make the AF to bulge on the inside and squeeze water out, breaking the lamellae sheets, progressively reducing the disc height, and eventually leading to disc collapse. This leads to increased transfer of more damaging axial loads to the vertebral body. Thus, a well hydrated NP is critical to the optimum mechanical performance of the disc because it moderates the transfer of energy from one vertebral body to another by lateral transfer of energy to the elastic AF and re-absorbs the energy on relaxation.

Human IVD degeneration usually begins early in the second decade of life progressing into late adult age [7]. Degeneration is initiated by PG aggrecans breakdown and gradually leaching out from the NP because of injury or disease [8]. The loss of the hydrophilic PGs with their associated negatively charged glycosaminoglycan (GAG) reduces the fixed charge density of the Nucleus Pulposus and the hydrating osmotic potential [7]. Reduction in hydration eventually leads to a reduction in hydrostatic pressure

Studies show that proteoglycan and water content in a disc decreases with age and degeneration [1]. When such a degenerate tissue is placed in a magnetic field, water molecules are observed to tumble at a much faster rate than when compared to a well hydrated disc [9]. These tumbling rates are exponential with time constants T1 due to energy loss to the tissue structure and T2 arising from energy changes due to dephasing between protons. The intensity of the induced signal due to equilibrium magnetization M_0 is lower for degenerate discs indicating the disc's lower state of hydration [10]. Thus, MR imaging could be used to measure change in water proton density because of decrease in hydration.

Physics of MR Imaging in biological systems

Spin is an intrinsic property observed in all odd atomic number or atomic mass nuclei. Simply, spin can be imagined as a circular periodic motion of a proton around its own axis with an angular momentum S. Since current is a charge in motion, by ampere's right hand rule a proton acquires a magnetic moment μ and has a north and south pole as demonstrated in Figure 2. Introduction to NMR Physics is discussed in Appendix A.

Hydrogen protons are abundant in tissue and when placed in a static magnetic field B_0, an ensemble of protons will precess around the axis of the magnetic field with a Larmor frequency v given by:

$$v = \gamma B_0 / 2\pi \quad (1)$$

where $\gamma/2\ \pi$ is the gyromagnetic ratio which is 42.58MHz/T for hydrogen.

A slight majority of protons with lower energy will align parallel to the magnetic field while the rest which are at a high energy level will align antiparallel to the main magnetic field Figure 3.

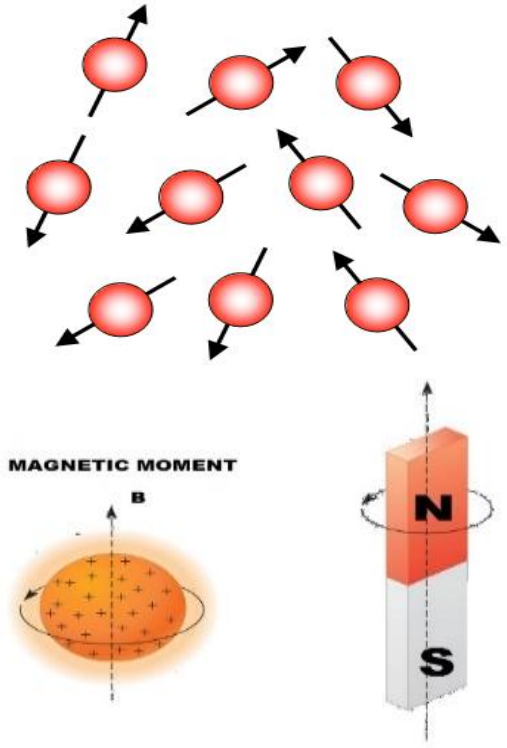

Figure 2. Protons in the absence and in the presence of magnetic field [reproduced from: http://physiology-physics.blogspot.com.au/2010/06].

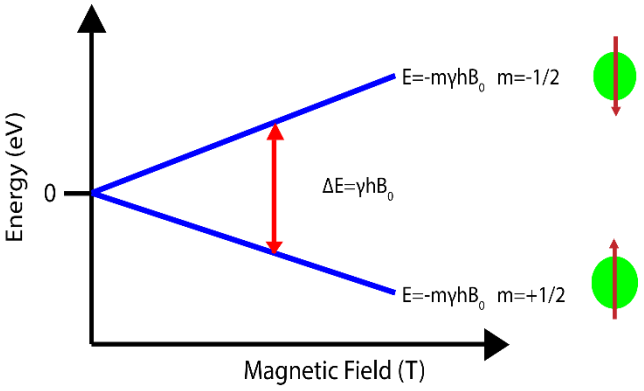

Figure 3. The two possible parallel and antiparallel orientations [reproduced from:http://chemwiki.ucdavis.edu/Physical_Chemistry/Spectroscopy/Magnetic_Resonance_Spectroscopies/Nuclear_Magnetic_Resonance].

The distribution of the protons in the parallel and antiparallel orientation is statistical with a Boltzmann distribution giving a net magnetization M_0 proportional to the population difference between the parallel and antiparallel energy levels given by:

$$\boldsymbol{M_o = M_z = \sum_{n=1}^{N_S} \mu_{z,n} = \frac{h\gamma}{4\pi}(N_{parallel} - N_{antiparallel}) = \frac{\gamma^2 h^2 B_0 N_S}{16\pi^2 KT}} \quad (2)$$

where h the planks constant(6.63×10^{-34}Js), K is the Boltzmann constant(1.38×10^{-23}J/K), T is temperature (K) and $N_{Parallel}$ and $N_{antiparallel}$ is the number of protons in the respective energy states, and N_S is the total number of proton nuclei in the sample [11]. Because of the high B_0, the signal is not easily detectable in the longitudinal direction thus the net magnetization vector is rotated from the longitudinal z axis to the transverse x,y plane to enable signal detection. This is done by applying a radiofrequency pulse signal with Larmor resonance frequency, $\nu = \gamma B_0 / 2\pi$. The RF magnetic component B_1 produces a torque which flips the net magnetization to the transverse plane by causing the low energy protons to transit to the high energy level. The protons precess around the B1 axis with frequency $\nu_1 = \gamma B_1 / 2\pi$ as well as around the B_0 axis with frequency $\nu = \gamma B_0 / 2\pi$. The protons in the transverse plane are now in phase and they precess coherently in the transverse plane at Larmor frequency.

Signal Detection

Faraday's law states that the induced voltage in a coil is proportional to the rate of change of magnetic flux with time inside the coil. If a coil is placed in the transverse plane after an RF pulse, the processing protons will induce a voltage in the coil that is proportional to B_0,and is given by:

$$\boldsymbol{E \propto -\frac{d\emptyset}{dt}} \quad (3)$$

where $\emptyset$ is the magnetic flux density through the cross-sectional area of the MR detector coil.

Spin Relaxation

The RF pulse in flipping the net magnetization M_z from its equilibrium M_0 value makes the M_x and My components to rise from zero to a maximum when the net magnetization is in the x, y plane. In the x, y plane, $M_z = 0$ and $M_x = M_y = M_0$. At the end of the pulse, all the magnetization components start to relax back to their equilibrium values. The relaxation is induced by: (i) resonance of nuclear spin and bio system lattice thermodynamic motion and (ii). Proton exchange. The longitudinal relaxation is which is energy exchange between nuclei and lattice known as spin-lattice relaxation is controlled by the time constant T_1. The transverse or spin-spin relaxation controlled by the time constant T_2.

The time evolution of the spin-lattice and Spin-spin relaxations are described by the Block equations [12]:

$$\frac{\boldsymbol{dM_x}}{\boldsymbol{dt}} = \boldsymbol{\gamma M_y \left(B_0 - \frac{\omega}{\gamma}\right) - \frac{M_x}{T_2}})$$

$$\frac{\boldsymbol{dM_y}}{\boldsymbol{dt}} = \boldsymbol{\gamma M_z B_1 - \gamma M_x \left(B_0 - \frac{\omega}{\gamma}\right) - \frac{M_y}{T_2}})$$

$$\frac{\boldsymbol{dM_z}}{\boldsymbol{dt}} = \boldsymbol{-\gamma M_y B_1 - \frac{M_z - M_0}{T_1}} \quad (4)$$

These Bloch's equations have solutions:

$M_x(t) = [M_x(0)\cos(\omega ot) + M_y(0)\sin(\omega_o t)]e^{-t/T_2}$

$M_y(t) = [M_o \sin(\omega ot) - M_y(0)\cos(\omega_o t)]\, e^{-t/T_2}$

$M_z(t) = [M_z(0) - M_o]e^{-t/T_1} + M_o \quad (5)$

where M_x, M_y and M_z are the magnetizations components as observed from the reference frame, and ω_o is the rotational angular frequency about the main magnetic field.

Spin-Lattice (T_1) Relaxation

T_1 relaxation occurs when the longitudinal magnetization M_z component grows back to the equilibrium magnetization M_0 and in the process releasing the energy that was initially absorbed from the RF pulse to its immediate environment. The T_1 relaxation time is the time taken for the longitudinal magnetization Mz to regain 63% of equilibrium magnetization M_0. T_1 recovery is dependent on tissue environment.

T_1 is measured by means of saturation recovery where an application of a 90° pulse which is followed by delay time τ then 90° pulse which is immediately followed by acquisition. Alternatively, acquisition can be by inversion recovery where an application of a 180° pulse which is followed by delay time τ then 90° pulse which is immediately followed by acquisition. This process is

repeated with different delay times. The saturation recovery measured signal is given by:

$$\boldsymbol{S(\tau_n)} = \boldsymbol{M_0}\,(\mathbf{1} - \boldsymbol{e^{-\tau_n/T_1}}) \quad (6)$$

While the inversion recovery signal is given by:

$$\boldsymbol{S(\tau_n)} = \boldsymbol{M_0}\,(\mathbf{1} - \mathbf{2}\boldsymbol{e^{-\tau_n/T_1}}) \quad (7)$$

In both methods plotting ln ($\boldsymbol{S(\tau_n)}$) against $\boldsymbol{\tau_n}$ gives a straight line with slope $-T_1$ [11].

Variations in T1 between different tissues reflect the state of magnetization at a particular instant. The signal acquired is proportional to the state of magnetization at that instant during longitudinal relaxation. T_1 weighted images are achieved by manipulating the differences in signal intensities at any time during longitudinal relaxation with aim of getting high signal contrast between tissues. Tissues with short T_1 will attain longitudinal equilibrium faster and will have a higher magnetization with an associate stronger signal and the image generated is usually brighter. TR is the repetition time and is the duration between the beginning of longitudinal relaxation and the instant when longitudinal magnetization is measured. A longer TR diminishes contrast.

Spin-Spin Relaxation

The transverse relaxation T_2 occurs due to loss of proton phase coherence because of proton-proton repulsion forces. The repulsive forces de-phases the protons reducing the induced signal with time. A homogenous sample gives a spectral line width of $1/\pi T_2$. This is an Ideal case because the transverse decays at a much higher rate. The inherent inhomogeneity in the external magnetic field broadens the spectrum by a factor of $\frac{\mathbf{1}}{\boldsymbol{\pi T_2^*}}$ [13].

Measuring the value of T_2 involves the application of spin echo technique. Here a 90° pulse is applied followed by a delay time $\boldsymbol{\tau}$, then a 180° pulse is applied which is again followed by the time delay $\boldsymbol{\tau}$. This is then followed by acquisition [14].

If the procedure is repeated for n different values of $\boldsymbol{\tau}$ then

$$\boldsymbol{S(\tau_n)} = \boldsymbol{M_0}\,\boldsymbol{e^{-2\tau_n/T_2}} \quad (8)$$

Plotting ln $\boldsymbol{S(\tau_n)}$ against $\boldsymbol{2\tau_n}$ gives a straight line with slope $-1/\boldsymbol{T_2}$. T2 contrast is achieved by having long echo times [11].

As with T1 recovery, different tissues have different spin-spin relaxation constants, and these differences can be manipulated to achieve an image contrast. A comprehensive discussion on relaxometry imaging is given by Carneiro [15].

Material and Methods

In this study, sample of hydrogel and oxtail NP was subjected to increase in the hydrostatic pressure by way of compression of the sample. The aim was to increase sample activation energy and as a consequently also its rotational correlation time and measure observed changes in relaxation rates. The change in relaxation rates between compressed and uncompressed states was then measured by NMR relaxation imaging and results validated by NMR spectroscopy.

Uncompressed Sample Preparation

A Davis Gelatine hydrogel (Davis gelatine (NZ) Ltd.) 90% w/w water and 10% w/w gelatine was melted. The liquefied gel was then drawn into a 1mm plastic syringe to a height of 1.5cm. The adaptor end of the syringe was then melted to secure the gel inside the syringe. The gel was then allowed to resolidify.

Investigation on oxtail NP began with fresh oxtail being obtained from a local abattoir; fat tissue and muscle were then trimmed off to the vertebral body in order to access the disc. The vertebral body was dissected from the disc by severing it from the vertebral end-plate using a scalpel. The end plate was then removed to access the NP which was then excised and separated from the AP by using a scalpel and put into a glass jar. Care was taken to limit sample dehydration during preparation. The samples were then stored in a freezer at -18°C for 1 week during which period hydrogel measurements were carried out. A day prior to oxtail NP measurements, the NP was thawed in a refrigerator for 24 hrs and afterwards for 2 hours at room temperature before measurement was started.

The two samples of hydrogel and oxtail Nucleus Pulposus were then separately inserted into the barrel of the syringe care being taken to ensure that minimum air bubbles were in the syringe before sealing the adaptor end as shown in Figure 4. The syringe was then inserted into a 1.0 cm bore of bird cage receiver/transmitter RF coil and centred Figure 5b. The sample was then transferred to a 7.0 Tesla Bruker Avance 200 Digital NMR

(Bruker BioSpin MRI GMBH) scanner for T_1 and T_2 measurements.

Compression Sample Preparation

Compression was done using Instron 5544A Compression machine (Instron Pty Ltd.) USA stationed in the biomedical laboratory at Queensland University of Technology. To maintain the compression at 4.44 Atm. the adaptor end of the syringe for oxtail NP study was sealed using UHU super glue while the plunger seal was held in position by using Selleys Araldite epoxy resin (Selleys New Zealand). The sample was transferred back to the MRI lab for compressed measurement of T_1 and T_2 mapping.

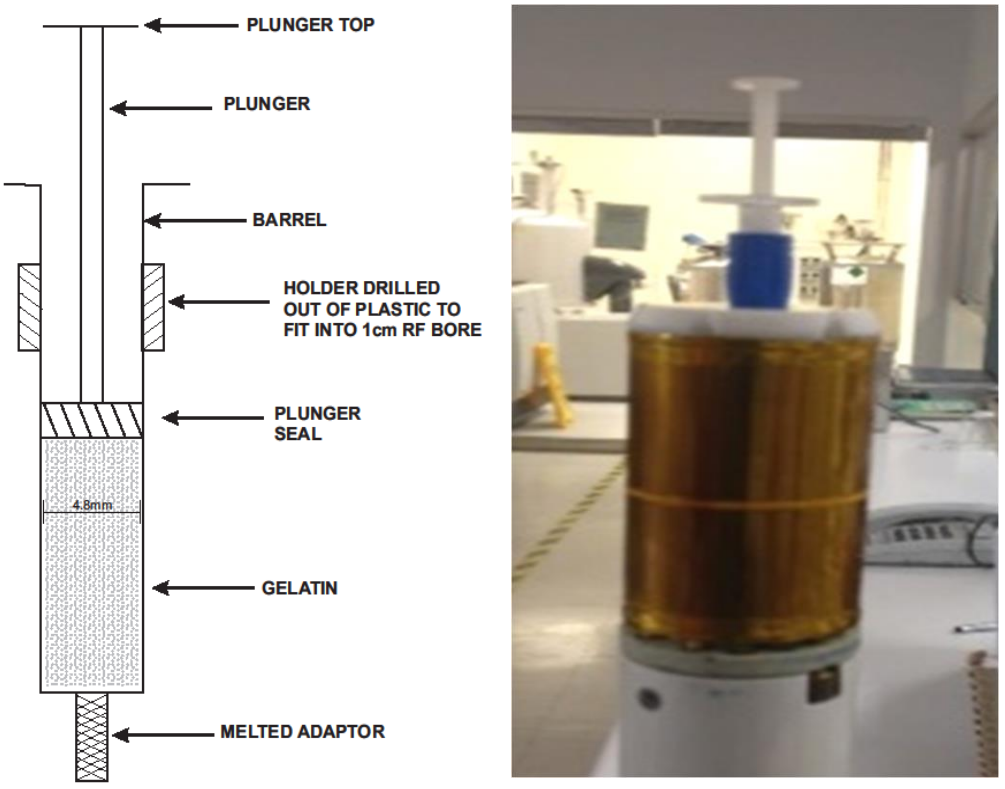

Figure 4. Schematic diagram of the hydrogel in the syringe and right the picture of the syringe inserted into the bird cage RF coil.

Spectroscopic R1 and R2 measurements

An initial estimate of the uncompressed state T_1 and T_2 relaxation times were acquired by Inversion recovery and Hahn echo techniques respectively [14]. Free induction decays acquired were then Fourier transformed and the area within the Fourier spectrum showed the amount of magnetization remaining after the polarising pulse. The areas were then plotted as a function of time and the decay constant for T_1 and T_2 estimated from 63.2% and 36.7% of net magnetization respectively. These measurements were used as a guide to set the TR and TE for subsequent R1 and R2 relaxation measurements with requirements being TR>3T1 and TE to be slightly greater than T_2. Then the spectrum was analysed to calculate the relaxation rates. Spectral analysis, integration and least square fitting was carried out using custom-made Mathematica 4.1 (Wolfram Research, Inc.) [16]. R1 studies were fitted to equation 9. while R2 studies were done by fitting to equation 10:

$$SI(T1) = -SI(0)EXP-(R_1 t) + C \quad (9)$$

$$SI(T2) = SI(0)EXP-(R_2 t) + C \quad (10)$$

SI is the signal intensity due to net magnetization, (R1) is the Spin lattice relaxation rate which is the inverse of T_1; t is the repetition time (TR) and C is a constant net magnetization M_0 signal. The relaxometry parameters were calculated by curve fitting on a voxel-by-voxel basis the intensity decay at each point in the ROI to single exponential curve fit according to χ^2 minimization algorithm and 95% confidence level.

R1 Measurements (Compressed and Uncompressed States)

A series of 64 axial T1 weighted images of a single axial slice of 0.5mm thickness were acquired for the uncompressed sample in a field of view of 128mm x 128mm. The acquisition matrix was 128 x 128 pixels. The RF pulse was a sync 3 type. The voxel size was 1mm x 1mm x 0. 5mm.The echo time (TE) was 6mS with two echoes per repetition time. There were 32 different repetition times (TR) used. A total of 64 images were acquired as shown in Table 1. below. The sequence of TR was in descending order from 10,000mS to 400mS.

The ROI was selected as a circular region of 3.6mm diameter centred within the axial slice but not in contact with the edge of the slice Fig. Oxtail NP image was inhomogeneous and ROI was chosen base. The average relaxation rates were then extracted from this ROI. The relaxometry parameter R1 was then estimated by fitting the simulated data using a single exponential least square curve fit by χ^2 minimization algorithm and 95% confidence.

R2 Measurements (Compressed and Uncompressed States)

A series of 100 axial T_2 weighted images of a single axial slice of 0.5mm thickness were acquired for the uncompressed and compressed sample in a field of view of 128mm x 128mm. The acquisition matrix was 128 x 128 pixels. The RF pulse was a sync 3 type. The voxel size was 1mm x 1mm x 0.5mm. The echo time (TE) was 6mS and the repetition time was 4000ms.

Spectroscopic Results

Free induction decays were acquired and then Fourier transformed. The area within the Fourier spectrum showed the amount of magnetization remaining after each polarising pulse. The areas were then plotted as a function of time and the decay constant for R1 and R2 were calculated by least square fitting to equation 8. and 9 respectively. Spectral analysis, integration and least square fitting were carried out using custom-made Mathematica 4.1 (Wolfram Research, Inc.). Compressed state measurements were carried out in a similar manner. The results are highlighted in Table 1.

Hydrogel Spectroscopic Results

The spectroscopic uncompressed T_1 was measured to be to be 1.35±0.002sec and that of T_2 was 79.0±1.2ms. The compressed state T_1 and T_2 spectroscopic estimates were calculated as 1.38±0.002s and 78.5±1.2ms respectively. There are no significant variations between compressed and uncompressed states.

Oxtail NP Spectroscopic Results

The spectroscopic uncompressed state measurement of the T_1 was 1.60±0.016sec and that of T_2 was 71.0±2.0ms. The compressed state T_1 and T_2 spectroscopic estimates were calculated as 1.62±0.005 sec and 73.0±0.6ms respectively shown below.

Hydrogel Relaxation Imaging

For T_1 mapping, a series of 64 consecutive images of the axial slice were acquired for both the compressed and uncompressed state of sample. Figure 8a. shows that the intensity of pixels increasing with increase in TR. This goes on to a maximum and then levels off at TR=5T1.

For T_2 mapping, a series of 100 consecutive images of the axial slice were acquired for the compressed and uncompressed state of sample. Figure 7 shows that the intensity of the first image pixels was the brightest and the pixels of the subsequent images had decreasing intensities with increase in TE.

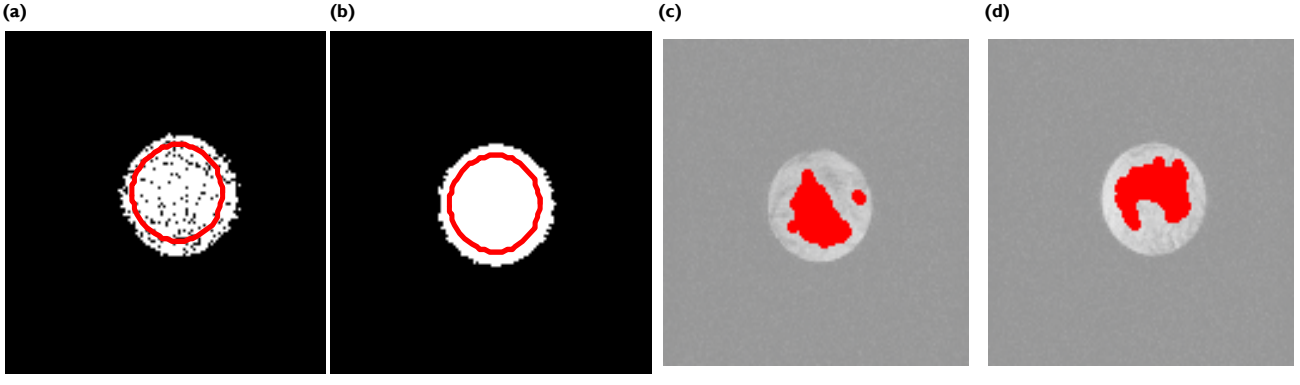

Figure 5. Spatial representation of selected regions of interest for. Images (a) and (b) represent the uncompressed and compressed ROIs in hydrogel sample while images (c) and (d) are for oxtail NP sample respectively.

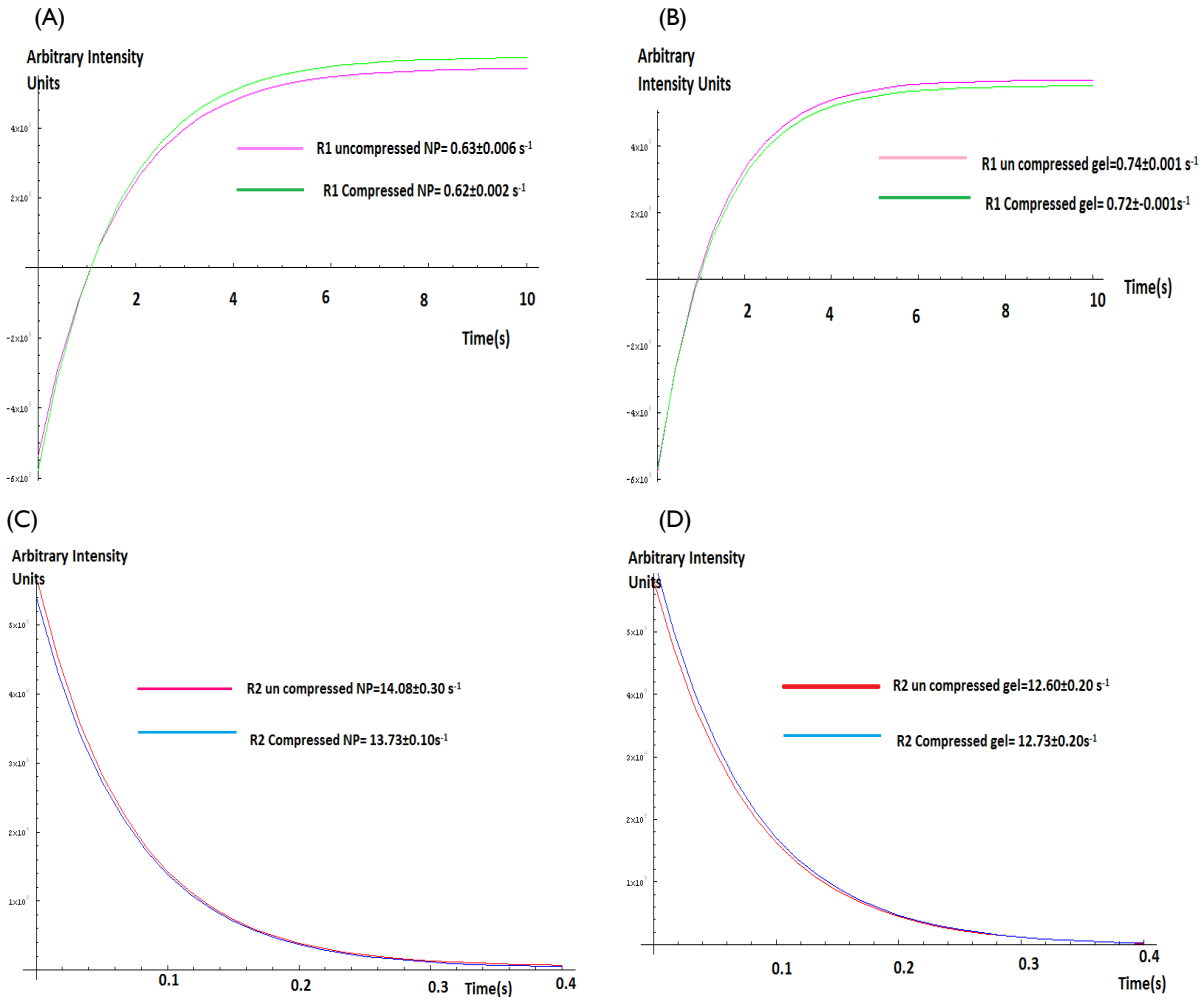

Figure 6. Spectroscopic relaxation curves for hydrogel and oxtail.

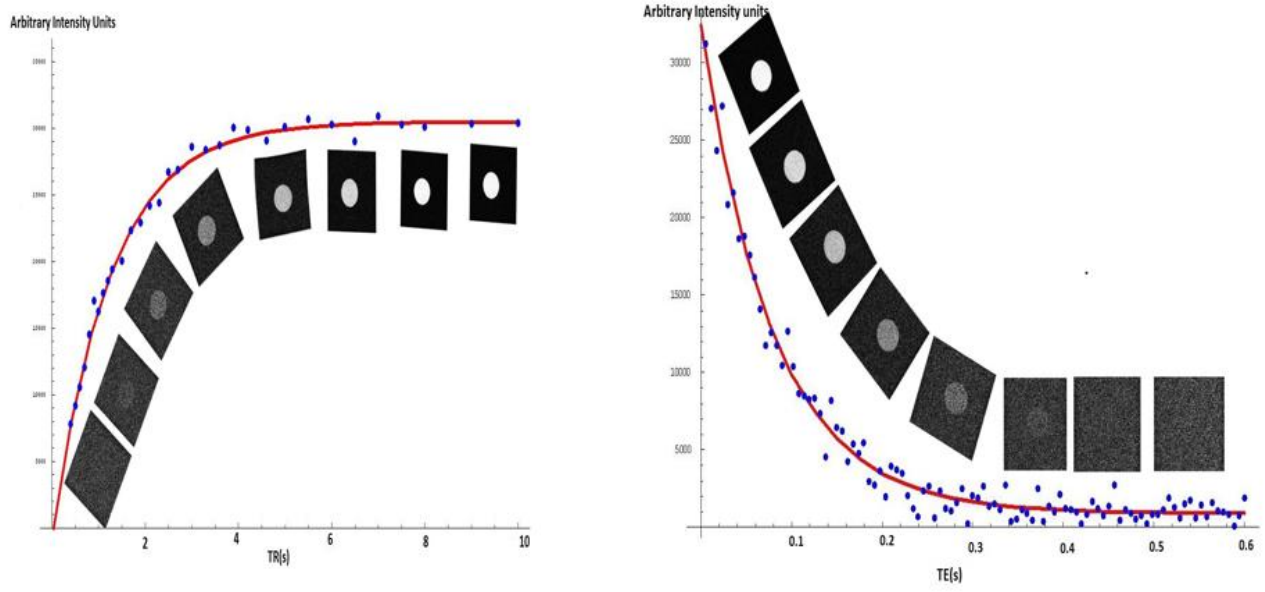

Figure 7. Illustration of the relaxation in a single voxel and the pictures represent the appearance of weighted relaxation images at respective time points.

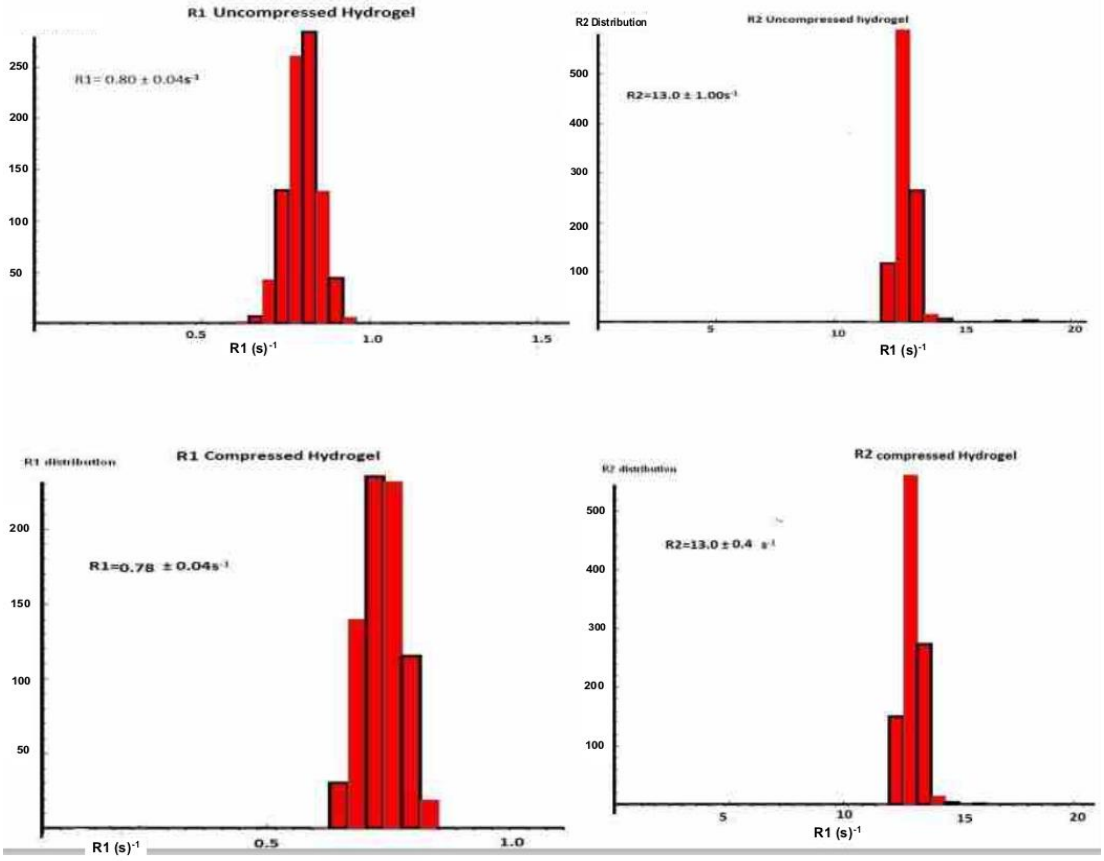

Figure 8. Histogram of hydrogel pixel density in selected ROI.

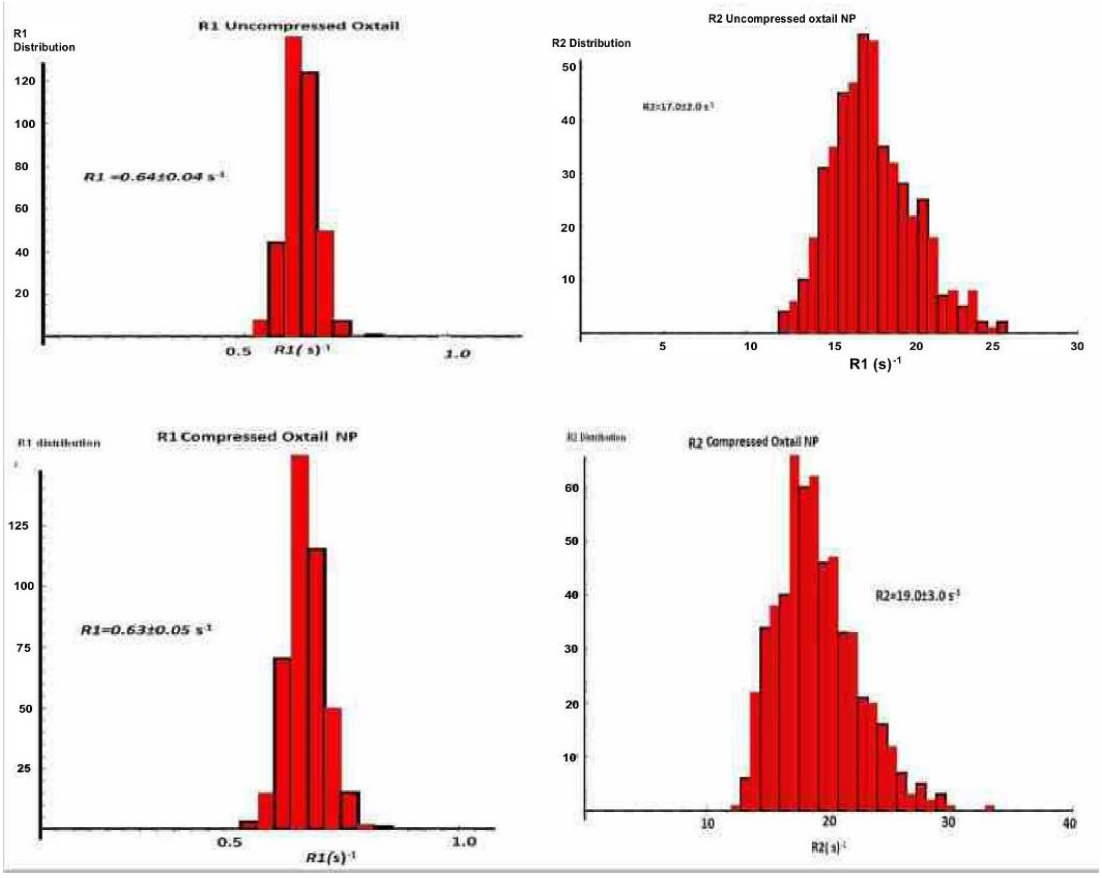

Figure 9. Histogram of oxtail NP pixel density in selected ROI.

Table 1. Summary of the longitudinal and transverse relaxation rates for both the uncompressed and compressed state of the 10% hydrogel gel sample and oxtail NP obtained from spatially resolved relaxation rate mapping

Hydrogel Sample Measurements					
Measurement Type	**Sample State**	**R1 (s^{-1})**	**T_1 (s)**	**R2 (s^{-1})**	**T_2(ms)**
Spectroscopic Measurements	**Uncompressed**	0.74±0.001	1.35 ± 0.002	12.60±0.20	79.40 ±1.20
	Compressed	0.72±-0.001	1.38 ±0.002	12.73±0.20	78.50 ±1.20
Relaxation rate by mapping	**Uncompressed**	0.80 ± 0.04	1.25 ±0.060	13.0 ± 1.00	76.9 ± 6.00
	Compressed	0.78 ± 0.04	1.28 ± 0.070	13.0 ± 4.00	76.9 ± 2.00
Oxtail NP Measurements					
Spectroscopic Measurements	**Uncompressed**	0.63±0.006	1.60±0.016	14.08±0.3	71.0±2.00
	Compressed	0.62±0.002	1.62±0.005	13.73±0.1	73.0±0.60
Relaxation rate by mapping	**Uncompressed**	0.64±0.04	1.56±0.10	17.0±2.0	58.8±7.0
	Compressed	0.63±0.05	1.59±0.10	19.0±3.0	52.6±8.0

A histograms representation of the distribution of R1 and R2 values for both the uncompressed and compressed state of the hydrogel sample is shown in figure 8 below. The T1 uncompressed and compressed measures were 1.25±0.06s and 1.28±0.07s respectively. T2 results were 76.9±60ms and 76.9±2.0ms respectively for uncompressed and compressed states respectively. It can be observed that variation in distributions is statistically insignificant. Measurement results are highlighted in Table 1.

Oxtail NP Results: Relaxation Imaging Measurement

For T1 mapping a series of 64 consecutive images of the axial slice were acquired for both the compressed and uncompressed state oxtail NP sample. Like hydrogel measurements, the R1 imaging shows an increase in intensity with increase in repetition time while in R2 measurements there is a decrease in intensity with increase in echo time TE. From Figure 10 shown below, it is observable that there is greater variance in the distribution when compared with the hydrogel samples in corresponding states. Also, there is greater variance in T_2 measurements when compared to T_1 measurements. Measurement results shows that T_1 for uncompressed and compressed states are 1.56±0.10s and 1.59±0.1s respectively while for T_2 they are 58.8±7.0ms and 52.6±8.0ms for the uncompressed and compressed states respectively. The results are summarized in Table 1.

Discussion

Magnetic Resonance in Heterogeneous Biological systems

Many biological systems are composed of both solid matrix macromolecules and liquid water. While water has a distinct narrow, single-line spectrum, the solid macromolecules have a very wide linewidth and very small amplitude in the noise domain which makes it difficult for detection. The high concentration of water molecule with respect to the macromolecules only compounds the situation. In heterogeneous bio systems such as IVD, it becomes difficult to quantify the macromolecules that make up the NP (proteoglycans).

The Protein macromolecules (PG) are solids with wide line-width spectrums and very small amplitude for conventional detection. Detection can only be by indirectly studying the relative changes in relaxation rates on surrounding water due to PG loss [17]. The PG have core protein linked to glycosaminoglycan's which have COO^{-1} and SO_3^{-1} binding sites for water molecules. This creates a hydration layer of motionally restrained water molecules around the macromolecules. The hydration layer molecules interact with and restrain free water molecules. This is accompanied with fast chemical exchange between the bound and free water Eqn. 11. Reduced motion means there is a higher probability that water protons will lose coherence faster (reducing T_2) and there will be more efficient loss of absorbed energy to lattice structure (reducing T_1) [17].

Magnetic motional averaging dominates the relaxation mechanics in free water with a correlation time of ~10^{-12}s. This contrasts with the more anisotropic bound water near the macromolecule which is only partially averaged through rapid exchange and diffusion of water molecules. The more restricted bound water has lower relaxation times reduced to ~ 10^{-6} s [18]. The chemical exchange between free and bound water in the hydration layer results in an effective relaxation rate given by [17, 18, 19]:

$$\boldsymbol{R1}_{\boldsymbol{eff}} = \left(\frac{\boldsymbol{1}}{\boldsymbol{T1}}\right)_{\boldsymbol{eff}} = \boldsymbol{X}_{\boldsymbol{f}}\left(\frac{\boldsymbol{1}}{\boldsymbol{T1}}\right)_{\boldsymbol{f}} + \boldsymbol{X}_{\boldsymbol{b}}\left(\frac{\boldsymbol{1}}{\boldsymbol{T1}}\right)_{\boldsymbol{b}} \quad (12)$$

where X_f and X_b are free and bound water fractions and $1/T1_f$ and $1/T1_b$ are their respective relaxation rates.

R2 contains a chemical exchange contribution [19]:

$$\boldsymbol{R2_{eff}} = (\frac{1}{T2})_{eff} = \boldsymbol{X_f}(\frac{1}{T2})_f + \boldsymbol{X_b}(\frac{1}{T1})_b + \boldsymbol{\pi X_f X_b}\,\Delta\boldsymbol{\omega^2\tau_{ex}} \quad (13)$$

where Δω is the difference in cyclic precession frequency between the bound and free water and $1/\tau ex = k+ + k-$.

The intrinsic rates are influenced by correlation time $\boldsymbol{\tau}$which is a function of activation energy [20]:

$$\frac{1}{T1} = \boldsymbol{C}(\frac{2\tau}{1+\tau^2\omega_0^2} + \frac{8\tau}{1+4\tau^2\omega_0^2}) \quad (14)$$

T_2 relaxation is more sensitive to slow exchanges and is given by:

$$\frac{1}{T2} = \boldsymbol{C}(\boldsymbol{3\tau} + \frac{5\tau}{1+\tau^2\omega_0^2} + \frac{2\tau}{1+4\tau^2\omega_0^2}) \quad (15)$$

where ω_0 is the resonance angular frequency, C= ($5.1x10^9$ s^{-2}) is a constant, $\boldsymbol{\tau}$ is the correlation time which is very small for pure water ($\sim\mathbf{5x10^{-12}s}$. For example in a 7T field and $\gamma B_0 / 2\pi$ = 298.06 MHz, substituting these values into equation 12 and 13 gives a value of T_2 =T1 =3.9s [20].

Research has also shown that MRI relaxation rates are sensitive to changes in pressure in biological systems such as IVD [21, 22]. However, it is still not clear whether this sensitivity is due to chemical changes due to loss of water from NP or it is due to hydrostatic pressure per se. In this study, it was hypothesised that MRI can exclusively detect changes in T_1 and T_2 due to hydrostatic pressure.

In this study both hydrogel and oxtail NP were subjected to compressive stresses and the change in their hydrostatic pressures observed. Because of the water–matrix coupling, disturbance of one parameter affects the other. It was thus thought possible, that by increasing the hydrostatic pressure, the activation energy of a biological system would increase and in effect also increase the molecular re-orientation and rotational correlation time hence causing detectable changes in relaxation rates.

However, most parts of the experimental results suggests that within physiological pressure alone, in the absence of compositional chemical changes, is not capable of inducing significant changes in relaxation rates. The hypothesis could thus not be fully supported by this research. A study of the results is discussed as follows.

Spectroscopic Relaxation Measurement

A look at the spectroscopic data in Table 1 shows there is no observable statistically significant differences in relaxation rates between the compressed and the uncompressed states in both hydrogel and oxtail NP measurements. The slight variations could be attributed to differences in manual shimming parameters carried out before sample state measurements [23]. These results might also be suggestive of the fact that the compressive load was not large enough to cause observable changes in relaxation.

Relaxation Imaging Results

Similar results to the spectroscopic study can be observed in hydrogel measurements where there is no statistically significant variations in T_1 and T_2 relaxations. An intriguing aspect of the study is observed in the oxtail NP imaging relaxation imaging results. The uncompressed T2 values are 58.8±7.0 ms while the compressed state T_2 values are 52.6±8.0 ms. These results might suggest that there is actually some biochemical or mechanical changes inside the confined NP when under compression which T2 relaxation measurement is sensitive to. Further investigations needs to be carried out to validate these results.

Probable reasons as to the variation between compressed and uncompressed states could be that there was bias in selection of ROI. Unlike in the more homogenous hydrogel, where a definite circle with a distinct radius from the centre of the syringe was chosen in both the compressed and uncompressed state, the oxtail NP is more heterogenous and a ROI selected in uncompressed state could not be reproduced after compression thus the sample measurements might have been carried out in different regions with different sizes and therefore could potentially be areas with different intensity distributions.

Another reason for the differences could be due to sample contamination during preparation. Separation of the NP from the inner AF was difficult to distinguish visually and therefore inner AF could have been trimmed into the sample reducing the effective T_2. Also, the sample could have been contaminated with blood which is high in iron. A previous study on liver, brain and spleen has shown that R2 is sensitive to Iron and the sensitivity increases

with increasing magnetic field [24, 25]. On compression, molecular motion of these contaminants could have diffused into the selected slice and and affected the results. Future studies might consider carrying out the measurements at different compression loads.

In general, it was observed that the T_1 relaxation for oxtail NP was 1.60 s which was much higher than that for hydrogel which was 1.35s. This could possibly be due to the fact that oxtail NP is populated by large poly diverse PG macromolecules and lower water content than hydrogel which makes it more viscous and have longer correlation times when compared with hydrogel [26, 27]. The reverse is true for T_2 relaxation, where oxtail NP T2 relaxation was 71ms compared to hydrogel at 78ms. This again can be explained by the differences in matrix concentration between hydrogel and oxtail NP. A past study showed that water content in NP of a calf ranged from 75% to 83% w/w [5]. The study also showed that there was a correlation of water content with T2 ($R2 = 0.81$, $P<0.001$). Suggesting that the low water to protein ratio favours lower T_2 relaxation with more weighting to the bound water which has a lower relaxation time (Equations 11 and 12) [19, 20, 28, 29]. At such low water to protein ratios , it is also probable that a chemical exchange environment is present between the hydration layer on and surrounding free water molecules which is in resonance with T_2 relaxation [30].

It is worthwhile to note that in comparison to hydrogel histograms, the oxtail NP histograms have a much wider spead from the mean as shown in Figures 9 and 10. This is attributable to the heterogeneity of the oxtail NP sample [31]. The non homogeneity could be due to both aggregating and more ubiquitous non aggregating PG which are more randomly distributed in the oxtail NP [23]. The PG are also of different sizes and which might explain the big variations in oxtail NP histograms intensities.

NMR Spectroscopy Vs NMR Relaxometry Imaging

It can also be observed that there are systemic differences in results between relaxation and NMR spectroscopic generated images.The relaxation image results were slightly lower than those due to NMR spectroscopy imaging. The variations might be due to better noise descrimination by relaxation imaging which minimize the influence factors [23].

Potential Sources of Error

In this study, the sample was held in a plastic syringe. Plastics are viscoelastic materials that could undergo deformation. It is possible that the plastic syringe deformed under pressure consequently reducing the hydrostatic pressure. Another possibility of loss of hydration pressure could be due to failure of glue used to secure the compression. As the glue sets, there is a possibility that it distorted and started relieving the pressure from the system. Future experimental setup might consider the use of more robust pneumatic glass tubes instead of syringe and glue. Pneumatic systems have valves which can maintain integrity under pressure.

A standard method for selecting ROI should be developed. This will ensure easier repeatability of the experiments. Clear procedures should be developed to reduce sample contamination. Future results might also consider working over a range of compressive stresses to be able to detect if there is a flow of impurities that might affect the results.

Conclusion

For most part of this study, results suggest that within physiological pressures alone, in the absence of compositional chemical changes, is not capable of inducing significant changes in relaxation rates. The outcome of this study is not conclusive and further studies are recommended to validate these results especially the unique findings attributed to changes in T_2 relaxations for oxtail NP . Future studies should also consider use of more robust pressure holding pneumatic systems to reduce any potential sources of error. The study shows great potential in quantifying the health of bilogical systems such as IVD. Degeneration could be arrested at infancy and interventional procedures initiated well in advance. Potential health problems such as back pains resulting from the grinding of vertebral bones and also sciatic pains due to herniated disc impinging on spinal nerve could be prevented the long before they start.This method can be used as a guide in selecting a treatment modality depending on the stage of degeneration. It could also find applications in emerging technologies such as design and developement of hydrogel scaffold materials in tissue engineering.

Abbreviations

IVD: Inter-vertebral disc; NP: Nucleus pulpous; GAG: Glycosaminoglycan; AF: Annulus Fibrosus; PG: Proteoglycans; MR: Magnetic resonance; NMR: Nuclear magnetic resonance; TR: Repetition time; TE: Echo time; ROI: Region of interest.

Author Contributions

All authors contributed to this study. All authors gave their final approval.

Competing Interests

We declare no competing interests.

References

[1] Nagashima, M., Abe, H., Amaya, K., Matsumoto, H., Yanaihara, H., Nishiwaki, Y., Toyama, Y. & Matsumoto, M. (2012). A method for quantifying intervertebral disc signal intensity on T2-weighted imaging. *Acta Radiologica*, *53*(9), 1059-1065.

[2] Bogduk, N. (2005). *Clinical anatomy of the lumbar spine and sacrum*. Elsevier Health Sciences.

[3] Buckwalter, J. A. (1995). Aging and degeneration of the human intervertebral disc. *Spine*, *20*(11), 1307-1314.

[4] Eyre, D., Benya, P., & Buckwalter, J. (1989). Intervertebral disc—Basic science perspectives. Chapter 5. *New Perspectives on Low Back Pain. Edited by JW Frymoyer, SL Gordon. Park Ridge, American Academy of Orthopaedic Surgeons*, 147-207.

[5] Marinelli, N. L., Haughton, V. M., Muñoz, A., & Anderson, P. A. (2009). T2 relaxation times of intervertebral disc tissue correlated with water content and proteoglycan content. *Spine*, *34*(5), 520-524.

[6] Urban, J. P., & McMullin, J. F. (1988). Swelling pressure of the lumbar intervertebral discs: influence of age, spinal level, composition, and degeneration. *Spine*, *13*(2), 179-187.

[7] Miller, J. A., Schmatz, C., & Schultz, A. B. (1988). Lumbar disc degeneration: correlation with age, sex, and spine level in 600 autopsy specimens. *Spine*, *13*(2), 173-178.

[8] Carragee, E. J., Don, A. S., Hurwitz, E. L., Cuellar, J. M., Carrino, J., & Herzog, R. (2009). 2009 ISSLS prize winner: does discography cause accelerated progression of degeneration changes in the lumbar disc: a ten-year matched cohort study. *Spine*, *34*(21), 2338-2345.

[9] Antoniou, J., Mwale, F., Demers, C. N., Beaudoin, G., Goswami, T., Aebi, M., & Alini, M. (2006). Quantitative magnetic resonance imaging of enzymatically induced degradation of the nucleus pulposus of intervertebral discs. *Spine*, *31*(14), 1547-1554.

[10] Hickey, D. S., Aspden, R. M., Hukins, D. W., Jenkins, J. P., & Isherwood, I. (1986). Analysis of magnetic resonance images from normal and degenerate lumbar intervertebral discs. *Spine*, *11*(7), 702-708.

[11] Webb, A. (2022). *Introduction to biomedical imaging*. John Wiley & Sons.

[12] Bloch, F. (1946). Nuclear induction. *Physical review*, *70*(7-8), 460.

[13] Levitt, M. H. (2013). *Spin dynamics: basics of nuclear magnetic resonance*. John Wiley & Sons.

[14] Hahn, E. L. (1950). Spin echoes. *Physical review*, *80*(4), 580.

[15] Carneiro, A. A. O., Vilela, G. R., De Araujo, D. B., & Baffa, O. (2006). MRI relaxometry: methods and applications. *Brazilian journal of physics*, *36*, 9-15.

[16] Wolfram, S. (1999). *The MATHEMATICA® book, version 4*. Cambridge university press.

[17] Fung, B. M. (1977). Proton and deuteron relaxation of muscle water over wide ranges of resonance frequencies. *Biophysical Journal*, *18*(2), 235-239.

[18] Bryant, R. G., & Korb, J. P. (2005). Nuclear magnetic resonance and spin relaxation in biological systems. *Magnetic resonance imaging*, *23*(2), 167-173.

[19] Momot, K. I., Powell, S. K., Mithieux, S. M., & Weiss, A. S. (2013). Biomechanics of synthetic elastin: Insights from Magnetic Resonance microimaging. In *Advanced Materials Research* (Vol. 699, pp. 457-463). Trans Tech Publications Ltd.

[20] Finch, E. D., & Homer, L. D. (1974). Proton nuclear magnetic resonance relaxation measurements in frog muscle. *Biophysical journal*, *14*(12), 907-921.

[21] Nguyen, A. M., Johannessen, W., Yoder, J. H., Wheaton, A. J., Vresilovic, E. J., Borthakur, A., & Elliott, D. M. (2008). Noninvasive quantification of human nucleus pulposus pressure with use of T1ρ-weighted magnetic resonance imaging. *The Journal of Bone and Joint Surgery. American volume.*, *90*(4), 796-802.

[22] Wang, C., Witschey, W., Elliott, M. A., Borthakur, A., & Reddy, R. (2010). Measurement of intervertebral disc pressure with T1ρ MRI. *Magnetic resonance in medicine*, *64*(6), 1721-1727.

[23] Nguyen, M. L., Willows, B., Khan, R., Chi, A., Kim, L., Nour, S. G., Sroka, T., Kerr, C., Godinez, J., Mills, M. & International Geriatric Radiotherapy Group. (2014). The potential role of magnetic resonance spectroscopy in image-guided radiotherapy. *Frontiers in Oncology*, *4*, 91.

[24] Hocq, A., Luhmer, M., Saussez, S., Louryan, S., Gillis, P., & Gossuin, Y. (2015). Effect of magnetic field and iron content on NMR proton relaxation of liver, spleen and brain tissues. *Contrast media & molecular imaging*, *10*(2), 144-152.

[25] Sprawls, P. (1987). *Physical principles of medical imaging*. Aspen Publishers.

[26] Bushell, G. R., Ghosh, P., Taylor, T. F. K., & Akeson, W. H. (1977). Proteoglycan chemistry of the intervertebral disks. *Clinical Orthopaedics and Related Research®*, (129), 115-123.

[27] Chatani, K., Kusaka, Y., Mifune, T., & Nishikawa, H. (1993). Topographic differences of 1H-NMR relaxation times (T1, T2) in the normal intervertebral disc and its relationship to water content. *Spine*, *18*(15), 2271-2275.

[28] Cooke, R., & Wien, R. (1971). The state of water in muscle tissue as determined by proton nuclear magnetic resonance. *Biophysical Journal*, *11*(12), 1002-1017.

[29] Xia, Y., & Momot, K. (Eds.). (2016). *Biophysics and Biochemistry of Cartilage by NMR and MRI (Chapter 3)*. Royal Society of Chemistry.

[30] Mathur-De Vre, R. (1980). The NMR studies of water in biological systems. *Progress in biophysics and molecular biology*, *35*, 103-134.

[31] Tourell, M. C., Kirkwood, M., Pearcy, M. J., Momot, K. I., & Little, J. P. (2017). Load-induced changes in the diffusion tensor of ovine anulus fibrosus: a pilot MRI study. *Journal of Magnetic Resonance Imaging*, *45*(6), 1723-1735.

Appendix

Appendix A: Basic MRI Imaging Physics

MRI Quantum Mechanical Description

An atom is made up of a central nucleus composed of protons and neutrons which is orbited by electron/s. A stable atom has an equal number of protons and neutrons. The protons inside the nucleus spin only about their own axis.

A spinning proton has spin angular momentum S and a moving charge will always have associated magnetic field thus the proton acquires a magnetic moment generating a magnetic field. Because the protons are many and in different states of energy, they are constantly in a state of constant repulsion.

The angular momentum of protons is quantised:

$$S = \frac{h}{2\pi}[I(I+1)^{1/2} \quad \text{(A1)}$$

h is Planck's with value 6.63 x 10^{-34} JS. The value of I is non nonzero for odd number of protons, odd number of neutrons or both. For hydrogen atom, I is ½ thus S is given by:

$$S = \frac{h}{2\pi}\frac{\sqrt{3}}{2} \quad \text{(A2)}$$

The magnetic moment is directly proportional to angular momentum by:

$$|\mu| = \gamma|S| \quad \text{(A3)}$$

where γ is the nuclear type characteristic gyromagnetic ratio. Because the spin angular momentum is quantised, so is the magnetic moment μ and it is given by:

$$|\mu| = \gamma|S| = = \frac{h\gamma}{2\pi}[I(I+1)^{1/2} \quad \text{(A4)}$$

For the hydrogen atom the magnetic moment is given by:

$$|\mu| = \frac{h\gamma\sqrt{3}}{4\pi} \quad \text{(A5)}$$

In the presence of a strong magnetic field B_0 the values of μ are defined using the magnetic quantum number given by:

$$|\mu_z| = \frac{h\gamma}{2\pi}m_I \quad \text{(A6)}$$

For hydrogen atom m_I has two values +1/2 and -1/2 giving:

$$|\mu_z| = \pm\frac{h\gamma}{4\pi} \quad \text{(A7)}$$

It is apparent that the from above equations that the magnetic moments are oriented at 54.7° to main magnetic field in the parallel and antiparallel energy states.

The relative numbers of protons in the parallel and antiparallel states is dependent on interaction between the magnetic moment and the main magnetic field.

$$E = -\mu_z B_0 \quad \text{(A8)}$$

Substituting for equation 7 gives:

$$E = \pm\frac{h\gamma B_0}{4\pi} \quad \text{(A9)}$$

The energy difference between the parallel and antiparallel configuration is given by:

$$\Delta E = \frac{h\gamma B_0}{4\pi} + \left(-\frac{h\gamma B_0}{4\pi}\right) = \frac{h\gamma B_0}{2\pi} \quad \text{(A10)}$$

Applying Boltzmann equation:

$$\frac{N_{antiparallel}}{N_{parallel}} = e^{-(\Delta E/KT)} = e^{-(h\gamma B_0/2\pi KT)} \quad \text{(A11)}$$

K is the Boltzmann constant of 1.38 x 10^{-23} J/K and T is temperature in Kelvins. By first order approximation $e^{-x} = 1 - x$. Therefore,

$$\frac{N_{antiparallel}}{N_{parallel}} = 1 - \frac{h\gamma B_0}{2\pi KT} \quad \text{(A12)}$$

which gives:

$$N_{parallel} - N_{antiparallel} = N_s\frac{h\gamma B_0}{2\pi KT} \quad \text{(A13)}$$

where N_s is the sum of all protons in the body approximated to be $Ns. \approx 2N_{parallel}$

Classical description

It becomes much easier to intuit the MRI sequences by classically analysing the magnetic field interactions with the protons. The application of a magnetic field to a sample of protons at 54.7° to the main magnetic field, will have the effect of tending to align the proton magnetic moments with the main magnetic moment B_0. In the process a torque C which is perpendicular to both the B_0 and μ is created.

$$C = \mu \times B_0 \; = \; i_N|\pi||B_0|\sin\theta \qquad \text{(A14)}$$

Given that torque is the rate of change of Spin angular momentum dS with time we have

$$c = \frac{dS}{dt} \; = \; \mu \; \times B_0 \qquad \text{(A15)}$$

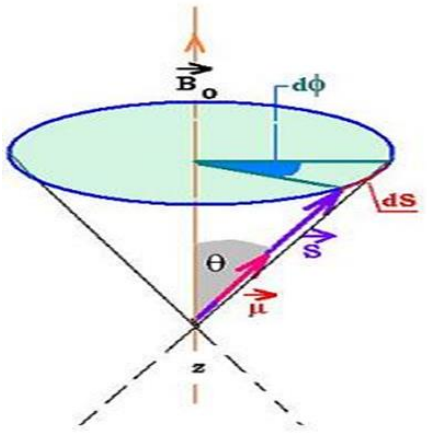

Figure A1. Classical torque of B_0 on μ. [Reproduced from: http://scientificsentence.net/Radiations/index.php?key=yes&Integer=nmr].

At infinitesimal time dt, the proton magnetic moment processes through a small angle $d\emptyset$ and in effect changing the spin angular momentum by dS:

$$\sin(d\emptyset) = \frac{dS}{|S|\sin(\theta)} = \frac{Cdt}{|S|sin\theta} \qquad \text{(A16)}$$

For infinitesimal time dt then $d\emptyset$ is also infinitesimal thus $\sin(d\emptyset) \sim d\emptyset$. But angular frequency is:

$$\omega = \frac{d\emptyset}{dt} = \frac{C}{|S|Sin\theta} = \frac{\mu \times B_0}{|S|sin\theta} \qquad \text{(A17)}$$

But $\mu = \gamma S$ substituting into the equation gives:

$$\omega = \frac{\gamma S \times B_0}{|S|sin\theta} \qquad \text{(A18)}$$

and expanding the vector cross product gives:

$$\omega = \frac{\gamma|S||B_0|sin\theta}{|S|sin\theta} = \; \gamma B_0 \qquad \text{(A19)}$$

Thus protons placed in a magnetic field will precess around the axis of that field with a frequency proportional to the magnitude of the magnetic field. This frequency is known as the Larmor frequency

A3. Creating an Image

In MR imaging, an image is usually a made up of a grid pixels representing a volume element in a tissue. The intensity of each pixel represents the level of magnetization in a given voxel.

An image is formed by selectively perturbing the magnetic homogeneity of B_0 by the introduction of gradient magnetic coils. The gradients causes variation in precessional frequency which enables the spatial determination of a signal source. The gradients are three dimensional in nature applied in the x,yand z directions respectively symbolized by the notations:

$$\frac{\partial B_Z}{\partial_Z} = \; G_{z,} \; \frac{\partial B_Z}{\partial_x} = \; G_{x,} \frac{\partial B_Z}{\partial_y} = \; G_{y,}$$

At the point where x, y and z = (0, 0, 0) , the magnetic field is B_0 with a resonant frequency ω_0 .All nuclei will then experience a magnetic field as a function of their position in the gradient:

$$B_{Z\,=} B_0 \; + ZG_Z \qquad \text{(A20)}$$

where G_Z has the units of tesla (T) per meter

As a function of position, the respective precessional frequencies can be established

$$\omega_z \; = \gamma B_z \; = \gamma(B_0 + zG_z) \qquad \text{(A21)}$$

which in a rotating frame becomes:

$$\omega_z = \gamma(zG_z) \quad \text{(A22)}$$

The same expressions can be established with the x and y directional gradients. Image formation is usually in three stages, i.e . Slice selection, frequency encoding and phase encoding.

Slice select gradient

A slice to be imaged is chosen by applying a sync pulse of defined band width frequency in the presence of a slice magnetic field gradient. Only those processing at frequencies within the bandwidth will achieve resonance and will flip to the transverse plane. The thickness of the slice is dependent on the frequency bandwidth and the slice select gradient chosen:

$$T = \frac{2\Delta\omega_s}{\gamma G_{slice}} \quad \text{(A23)}$$

The signal acquired is measured from the whole slice with no way of determining the signal variation with position:

$$S = \int_{slice}\int_{slice} \rho\,(x,y)dxdy \quad \text{(A24)}$$

where ρ (x,y) is the proton density.

Frequency Encoding

After the spin select gradient excitation, the slice select gradient is switched off. The protons as they decay they acquire the resonant frequency ω_0 as they will only be exposed to B_0. As the transverse magnetizations continues to decay, a gradient magnetic field is then applied perpendicular to the slice select direction. This causes the net magnetic field to vary linearly along the X direction. This creates a measureable difference in spins that varies with position thus frequency is encoded.

The signal measured is given by:

$$S(G_x, t_f) \;\alpha\; \int_{slice}\int_{slice} \rho\,(x,y)e^{-i\gamma G_x\, xt_f}dxdy \quad \text{(A25)}$$

Phase Encoding

A permanent change in phase is induced by applying a third magnetic field gradient G_{ph} along the y direction just immediately after the slice selection gradient. The protons will precess at a frequency given by:

$$\omega_y = \gamma(yG_y) \quad \text{(A26)}$$

This creates a signal which has a spatial dependence on phase shift. This change in shift varies with distance from the Isocentre:

$$(G_y, t_{ph}) \;\alpha\; \int_{slice}\int_{slice} \rho\,(x,y)e^{-i\gamma G_y\, yt}dxdy \quad \text{(A27)}$$

The frequency and phase encoding gradients have an effect on the signal given by

$$(G_y, t_{ph}G_x, t_f) \;\alpha\; \int_{slice}\int_{slice} \rho\,(x,y)e^{-i\gamma G_y\, yt}\, e^{-i\gamma G_x\, xt_f}dxdy \quad \text{(A28)}$$

K-Space

The process of acquisition is done at different phase encoding gradients which creates rows of spatially varying signal amplitudes measured over time. This set of data is in the time domain and is called K space. A Fourier transform operation is applied to the data set. This makes each cell to represent a signal amplitude with the rows and columns representing frequency as a function of rate of phase change and position respectively.

Appendix B. Images

Hydrogel Spectroscopic Relaxation Curves

Below shows the NMR Spectroscopic relaxation curves for Hydrogel. The variations in curve outline are negligible

Sample Compression

The sample in the syringe was compressed to 8N using Instron 5544A Compression machine (Instron Pty Ltd.) USA stationed in the biomedical laboratory at QUT.

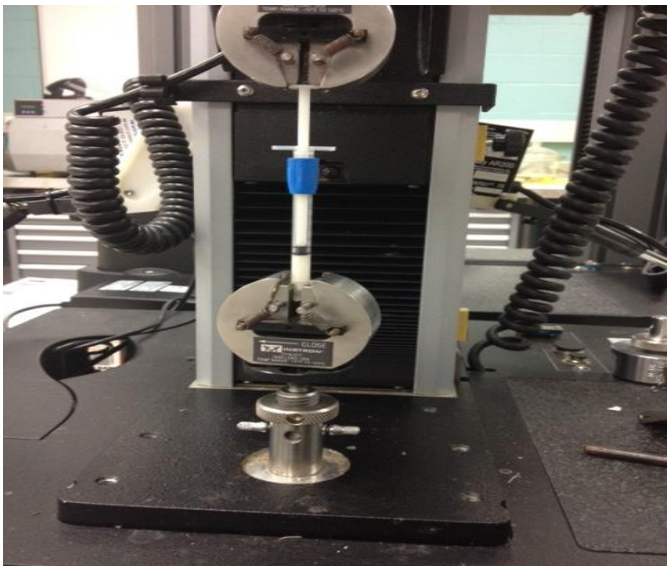

Figure B1. Sample compression.